Separation of diffracted waves in transversely isotropic media

YOGESH ARORA AND ILYA TSVANKIN

Center for Wave Phenomena, Colorado School of Mines, 1500 Illinois Street, Golden, CO 80401, USA (yarora@mymail.mines.edu)

Received: October 1, 2015; Revised: November 12, 2015; Accepted: April 28, 2016

ABSTRACT

Imaging diffracted waves can provide useful information about complex subsurface geology and fracture networks. Separation of diffractions from typically more intensive reflected events can be done based on specularity, which measures deviation from Snell's law. Here, we analyze two formulations of specularity and their applicability to diffraction processing in the presence of anisotropy. We show that the most common definition of specularity, originally introduced for pure modes in isotropic media, remains valid for both pure and converted waves in arbitrarily anisotropic models. The other formulation operates directly with the difference between the slowness projections onto the reflector for the incident and reflected waves. Testing on a VTI (transversely isotropic with a vertical symmetry axis) diffraction ramp model demonstrates that both formulations produce satisfactory results for anisotropic media with appropriate tapering of the specularity gathers. Then separation and imaging of diffractions is performed for the structurally complex VTI Marmousi model. We also analyze the sensitivity of diffractions in the specularity gathers to errors in the symmetry-direction velocity and anellipticity parameter η.

Keywords: diffraction, transverse anisotropy, Kirchhoff migration, specularity

1. INTRODUCTION

Diffractions are caused by heterogeneities with linear dimensions smaller than seismic wavelength. They can provide valuable information about complex subsurface features such as small-scale faults, fractures, pinch-outs, karst, and rough edges around the salt bodies (*Landa, 2010*). Diffractions are usually treated as noise during conventional seismic processing, which is designed for enhancing and imaging reflected waves.

One of the main challenges in utilizing diffractions is separating them from reflections, which typically dominate surface seismic data. *Khaidukov et al. (2004)* enhance diffractions in isotropic media by applying focusing and defocusing operators. *Fomel et al. (2007)* operate on poststack time sections to separate diffractions using plane-wave destruction filters and perform isotropic velocity analysis based on a measure of focusing. *Berkovitch et al. (2009)* present an application of a multifocusing technique in the context of diffraction separation. Imaging with diffractions can potentially provide higher-

resolution seismic sections (*Khaidukov et al., 2004*), which can be combined with conventional reflection-based images for improved interpretation (*Sturzu et al., 2013*; *Khaidukov et al., 2004*; *Moser and Howard, 2008*). Processing of diffraction-based images by evaluating the focusing measure can be used for fracture detection in azimuthally anisotropic media (*Al-Dajani and Fomel, 2010*). Moreover, diffractions can be used for anisotropic parameter estimation because they carry information from a wide range of dips (*Waheed et al., 2013a,b*).

Kozlov et al. (2004) applied a weighting function, based on the Fresnel zone around the specular reflected ray, to the Kirchhoff integral to suppress reflections during isotropic migration. However, constructing such weights for anisotropic media is cumbersome. *Moser and Howard (2008)* propose another approach (called "specularity"), which measures the deviation from Snell's law at the reflection point, to define the weighting function. This technique is used by *Sturzu et al. (2013)* to create "specularity gathers" for efficient separation of diffraction and reflection energy. Although specu larity ignores the fact that reflection events are produced inside a certain area (Fresnel zone) around the reflection point, specularity gathers overcome this problem and provide an efficient method of diffraction separation.

Here, we examine two formulations of specularity, one of which is new, and discuss their applicability for pure and converted waves in general anisotropic media. First, we study the response of these specularity expressions for a simple homogeneous isotropic model. Then performance of both formulations in separating and imaging of diffracted waves is illustrated on a VTI ramp model as well as on the more complex VTI version of the Marmousi model (*Alkhalifah, 1997*). Finally, we assess the sensitivity of diffractions in specularity gathers to errors in the velocity model.

2. THEORY

The Kirchhoff migration integral computes a stack over the diffraction hyperbola (*Schneider, 1978*). This stack can be restricted to the Fresnel zone (*Chen, 2004*) by applying a weight function which reduces aliasing in the depth image for coarsely sampled data. If the weight function is designed to suppress the contribution from inside the Fresnel zone, the Kirchhoff integral images nonspecular scattered energy (*Kozlov et al., 2004*). This weight can be formulated in terms of specularity, which represents a measure of deviation from Snell's law.

Moser and Howard (2008) define specularity $\overline{S}$ as the cosine of the angle θ between the sum of the source-side (subscript *s*) and receiver-side (subscript *r*) slowness vectors and the interface normal at the reflection point ($\boldsymbol{X}$) (Fig. 1):

$$\overline{S}\left(\boldsymbol{s}, \boldsymbol{r}, \boldsymbol{X}\right) = \cos\theta = \frac{\left(\boldsymbol{P}_s + \boldsymbol{P}_r\right)\cdot \boldsymbol{n}}{\left|\boldsymbol{P}_s + \boldsymbol{P}_r\right|}\ , \tag{1}$$

where $\boldsymbol{P}_s$ and $\boldsymbol{P}_r$ are the slowness vectors obtained from the derivatives of the source-side traveltime $T\left(\boldsymbol{s}, \boldsymbol{X}\right)$ and receiver-side traveltime $T\left(\boldsymbol{r}, \boldsymbol{X}\right)$, respectively, $\boldsymbol{s}$ is the source position, $\boldsymbol{r}$ is the receiver position, and $\boldsymbol{n}$ is the unit vector normal to the reflector

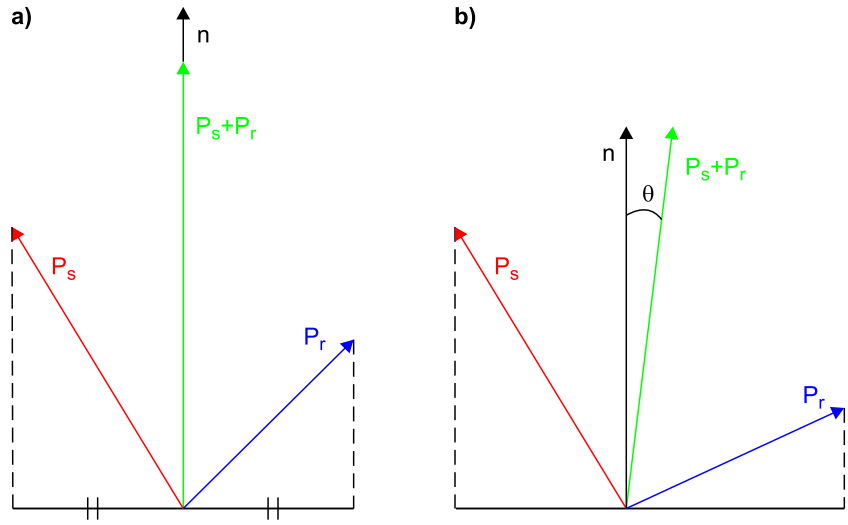

Fig. 1. Source-side slowness vector ($\boldsymbol{P}_S$), receiver-side slowness vector ($\boldsymbol{P}_r$), the sum of the two slowness vectors and the interface normal vector ($\boldsymbol{n}$) for **a)** a specular reflection, **b)** a nonspecular diffraction.

($\boldsymbol{n}$ can be computed from the conventional depth image). If we assume that the vectors $\boldsymbol{P}_s$ and $\boldsymbol{P}_r$ of the specular reflected ray point towards the surface, their projections onto the reflector should cancel out according to Snell's law. Therefore, the sum of these slowness vectors is always aligned with the interface normal for any specular event, which can represent a pure or a modeconverted wave. Therefore, although the formulation by *Moser and Howard (2008)* was designed for pure modes in isotropic media, it is entirely valid for arbitrary anisotropy and mode conversions. Alternatively, specularity can be defined directly through the projections of the source and receiver slowness vectors onto the interface (Fig. 1). To maintain consistency with Eq. (1), the normalized sum of these projections can be subtracted from unity:

$$\overline{S}\left(\boldsymbol{s},\boldsymbol{r},\boldsymbol{X}\right)=1-\frac{\left|\boldsymbol{P}_S\times\boldsymbol{n}+\boldsymbol{P}_r\times\boldsymbol{n}\right|}{\left|\boldsymbol{P}_S+\boldsymbol{P}_r\right|}\ . \tag{2}$$

The value of $\overline{S}$ in Eqs (1) and (2) is equal to unity for specular reflections, and is less than unity for nonspecular events (diffractions). However, reflection energy is formed inside the entire the Fresnel zone where specularity values are generally smaller than unity as well. Therefore, the direct application of a specularity-based weight to the Kirchhoff integral leads to inefficient separation of diffractions.

3. SPECULARITY GATHERS

To overcome this problem, *Sturzu et al. (2013)* suggest building specularity gathers which, in principle, are similar to surface-offset common-image-gathers (CIGs). The specular and nonspecular events in the data are sorted into gathers according to specularity values, and then a taper function is applied to mute reflections. Finally, stacking over the specularity produces a depth image solely from diffractions. This process is illustrated by the following equations:

$$V(\boldsymbol{X}, S) = \int U(t, \boldsymbol{s}, \boldsymbol{r})\, \delta\big(t - T(\boldsymbol{X}, \boldsymbol{s}, \boldsymbol{r})\big)\, \delta\big(S - \overline{S}\big)\, dt\, d\boldsymbol{s}\, d\boldsymbol{r}\ , \tag{3}$$

$$I(\boldsymbol{X}) = \int V(\boldsymbol{X}, S)\, dS\ , \tag{4}$$

$$D(\boldsymbol{X}) = \int w(\boldsymbol{X}, S) V(\boldsymbol{X}, S)\, dS\ , \tag{5}$$

where $V(\boldsymbol{X}, S)$ is a cube (in 2D) with specularity gathers, $I(\boldsymbol{X})$ is the conventional depth image, $D(\boldsymbol{X})$ is the depth image from diffractions, T is the traveltime from the source to the receiver through the reflection point $\boldsymbol{X}$ ($T(\boldsymbol{s}, \boldsymbol{X}) + T(\boldsymbol{r}, \boldsymbol{X})$), $\overline{S}$ is the specularity defined either in Eq. (1) or (2), $U(t, \boldsymbol{s}, \boldsymbol{r})$ is the recorded data, and $w(\boldsymbol{X}, S)$ is the taper function. We apply both definitions of specularity $\overline{S}$ (Eqs (1) and (2)) to separate diffractions using Eqs (3)–(5).

4. EXAMPLES

Synthetic data are generated using anisotropic pseudo-acoustic finite-difference code sfttifd2d, and unit normal vectors are estimated with code sfdip (both from MADAGASCAR). Traveltime tables are created using code rayt2dan, and specularity gathers are built by modified code sukdmig2d (both from SEISMIC UNIX). All codes employed in our work are open source.

4.1. Specularity analysis

First, we test the two definitions of specularity on the simple model of a homogeneous isotropic layers (Fig. 2). The specularity values are computed for reflection points along the interface at the depth $z = 2.0$ km. The specularity is equal to unity for the specular reflection, but it decreases at different rates for the two definitions (Fig. 2b). The faster decrease in specularity computed from Eq. (2) could cause more smearing in gathers along the specularity axis. Hence, the choice of the taper function $w(\boldsymbol{X}, S)$ in Eq. (5) should depend on the definition of specularity.

4.2. Diffraction ramp model

Next, we apply the two formulations of specularity to perform separation and imaging of diffractions for a model with a VTI diffraction ramp (Fig. 3a). The conventional depth

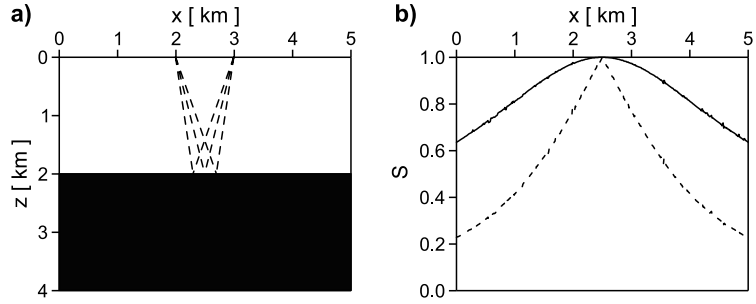

Fig. 2. **a)** Isotropic model with the source and receiver positions fixed at $x = 2$ km and $x = 3$ km, respectively. The reflection point is moved along the horizontal interface at a depth $z = 2.0$ km. The dashed lines represent ray pairs for the moving reflection point. **b)** The specularity (S) values obtained from Eq. (1) (solid curve) and Eq. (2) (dashed curve).

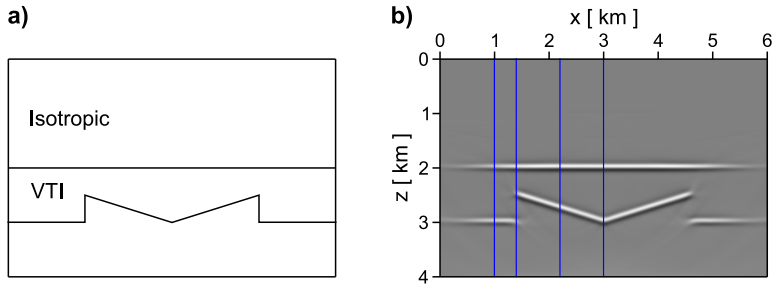

Fig. 3. **a)** VTI (transversely isotropic with a vertical symmetry axis) diffraction ramp model. The P-wave velocity in the top isotropic layer is 3.1 km/s and the Thomsen parameters of the VTI layer are $V_{P0} = 3.3$ km/s, $\varepsilon = 0.24$, and $\delta = 0.14$. **b)** The conventional depth (z) image of the model. Specularity gathers are computed at locations marked by the vertical lines.

image in Fig. 3b is generated with the actual velocity field, and specularity gathers are constructed at four locations along the line. There are no scatterers at locations $x = 1.0$ km and $x = 2.2$ km, so the corresponding gathers (Fig. 4a,c) have no diffracted energy at lower specularity values. However, the gathers contain significant nonspecular energy from the scatterers at locations $x = 1.4$ km and $x = 3.0$ km (Fig. 4b,d). As expected, gathers computed using Eq. (2) show more smearing of energy towards lower specularity values (Fig. 5). The adjustment of the taper function (Fig. 6), however, helps produce similar depth images (Fig. 7) from diffractions using both definition of specularity.

4.3. Sensitivity to model errors

Next, we analyze the sensitivity of diffractions in specularity gathers to errors in the velocity model. We use a homogeneous elliptical ($\eta = 0$) VTI medium with three point scatterers that represent perturbations in the velocity V_{P0} (Fig. 8). First, we increase V_{P0} by 500 m/s (about 16%), while keeping the other parameters at the actual values, and generate a depth image (Fig. 9a). As expected, the distortion in the V_{P0} causes defocusing

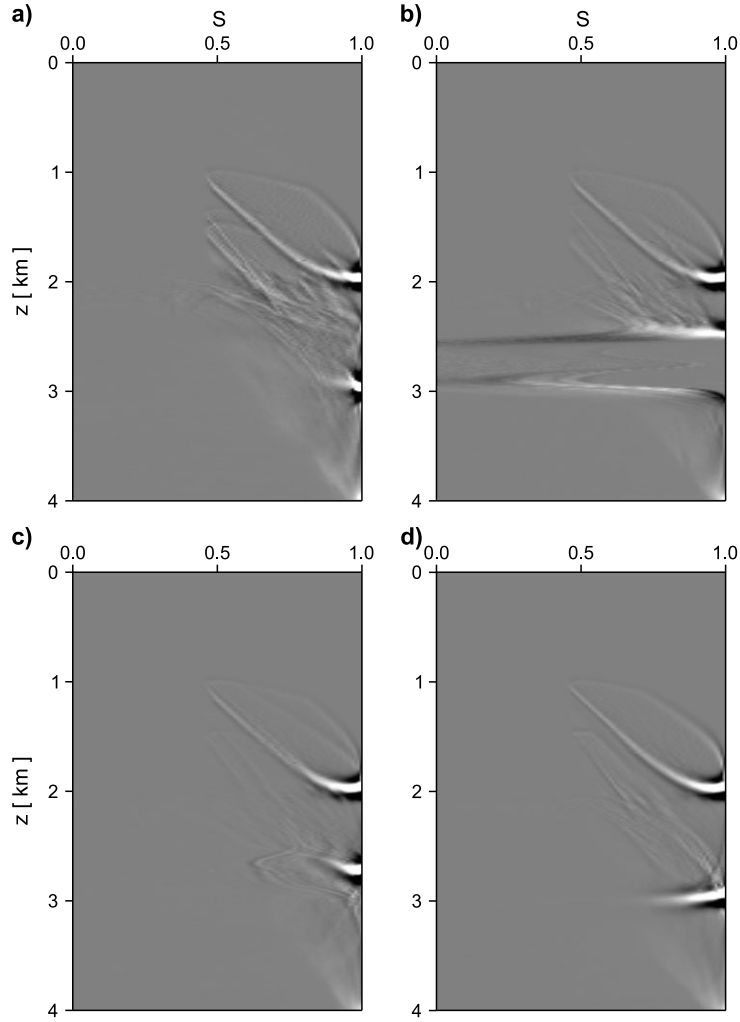

Fig. 4. Specularity (S) gathers generated using Eq. (1) for the model in Fig. 3a at locations **a)** x = 1.0 km, **b)** x = 1.4 km, **c)** x = 2.2 km, and **d)** x = 3.0 km.

of the scatterers (Fig. 9b). A specularity gather at location x = 3.0 km shows that the overstated V_{P0} causes bending of diffraction events (Fig. 10b). Next, we produce depth images (Fig. 9c–e) and specularity gathers (Fig. 10c–e) at the same location for distorted values of η. The diffraction in the specularity gather visibly bends even for $\eta = 0.09$, and the bending rapidly increases for larger η.

To get insight into these results, we compute diffraction traveltimes from the scatterer at location x = 3.0 km and depth z = 1.0 km for different values of η (Fig. 11) using the equation proposed by *Waheed et al. (2013a)*. Clearly, the influence of η on traveltimes

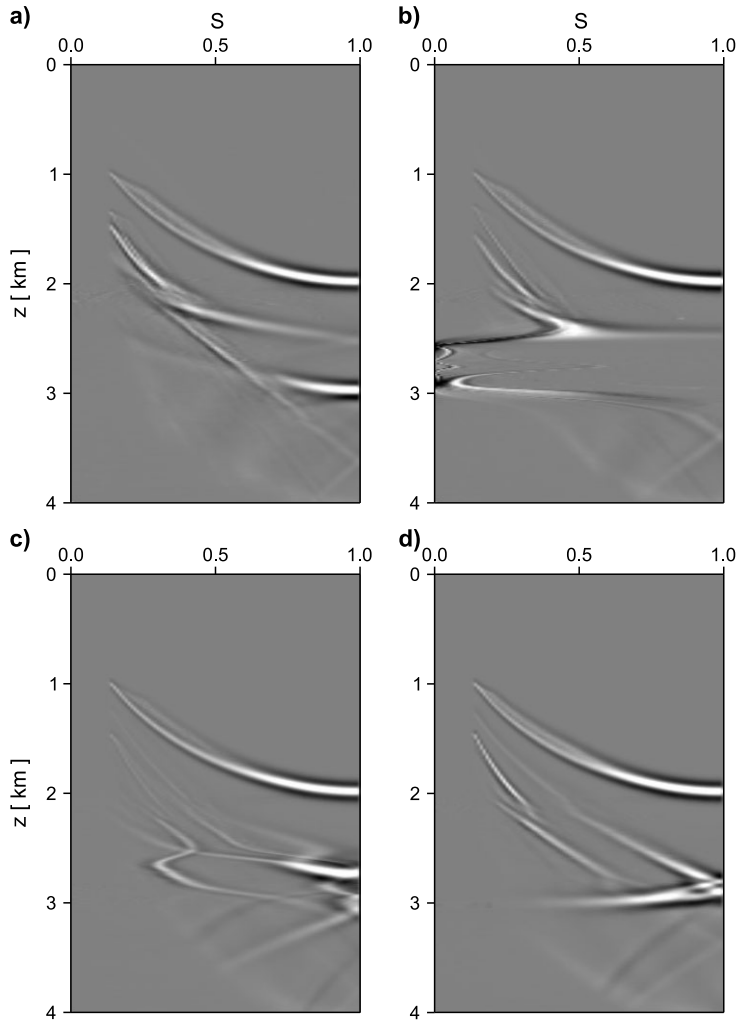

Fig. 5. Specularity (S) gathers generated using Eq. (2) for the model in Fig. 3a at locations **a)** x = 1.0 km, **b)** x = 1.4 km, **c)** x = 2.2 km, and **d)** x = 3.0 km.

increases with offset. Likewise, it is well known that the contribution of η to reflection moveout of horizontal events becomes more pronounced for long offsets. The deviation angle θ in Eq. (1) is equivalent to offset for diffractions (Fig. 1b), which implies that the specularity values are larger for near offsets. Therefore, it takes a pronounced distortion in η to cause bending of diffractions at higher specularity values (Fig. 10c–e).

4.4. VTI Marmousi model

To evaluate the performance of the algorithm for a more complicated structure, we carry out separation and imaging of diffractions for the anisotropic (VTI) version of the Marmousi model (*Alkhalifah, 1997*). This model has many scatterers created by

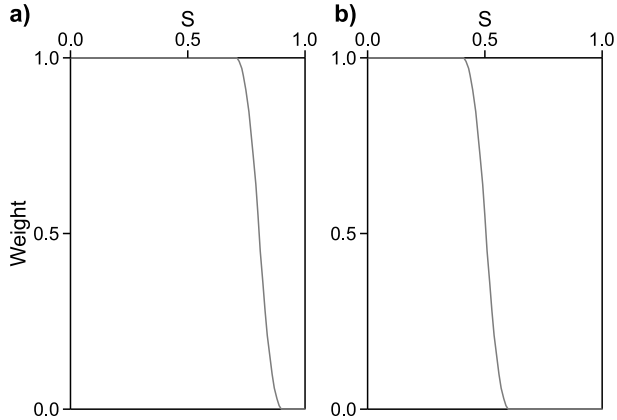

Fig. 6. Taper functions with muting starting at the following specularity values: a) $S = 0.70$, and **b)** $S = 0.40$.

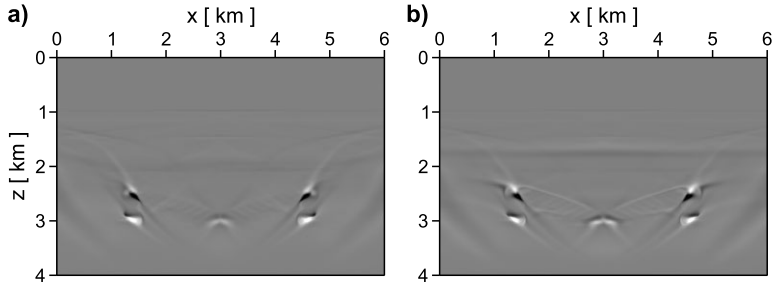

Fig. 7. Depth (z) images from diffractions obtained using the specularity defined using **a)** Eq. (1), and **b)** Eq. (2).

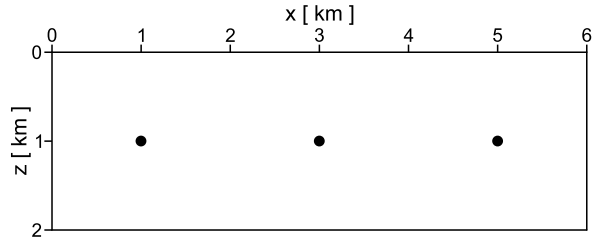

Fig. 8. Homogeneous VTI (transversely isotropic with a vertical symmetry axis) model with point scatterers marked by black dots. The model parameters are $V_{P0} = 3.0$ km/s, $\varepsilon = \delta = 0.18$ ($\eta = 0$).

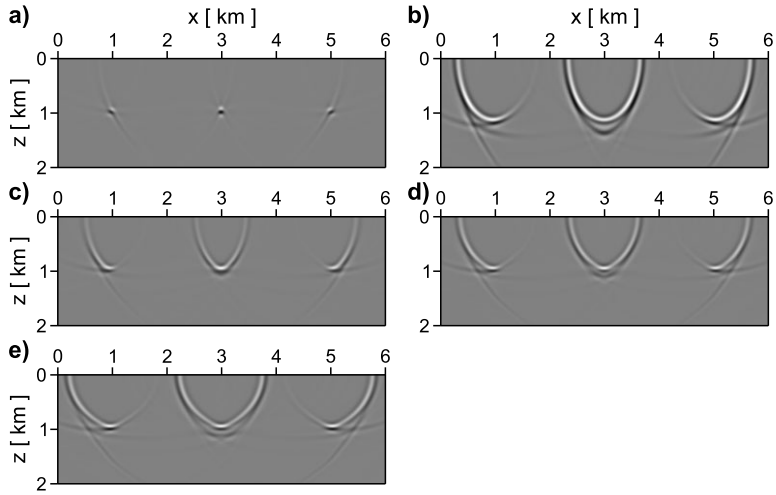

Fig. 9. Depth (z) images for the model in Fig. 8 obtained with **a)** the actual velocity field, **b)** the distorted $V_{P0} = 3.5$ km/s, **c)** the distorted $\eta = 0.09$ ($\varepsilon = 0.30$, $\delta = 0.18$), **d)** the distorted $\eta = 0.16$ ($\varepsilon = 0.40$, $\delta = 0.18$), **e)** the distorted $\eta = 0.24$ ($\varepsilon = 0.50$, $\delta = 0.18$).

intersections of faults and layer boundaries (Fig. 12), but these scatterers are not clearly visible in the conventional depth image (Fig. 13). We smooth the actual velocity field in Fig. 12 to generate traveltimes for the migration and separation of diffracted waves. The specularity gathers at location $x = 4.61$ km exhibit energy spread over all specularity values (Fig. 14). The taper function shown in Fig. 6b with muting starting at $S = 0.40$ is applied to the specularity gathers created using Eq. (1). The complexity of this model produces a "chaotic" specularity gather generated using Eq. (2) (Fig. 14b). Therefore, we process the gathers created with Eq. (2) using more severe tapering with muting starting at $S = 0$. Although the diffraction images in Fig. 15 are comparable, the scatterers look brighter in the image generated with Eq. (1) (Fig. 15a). The dimming in the depth image obtained with Eq. (2) (Fig. 15b) is caused primarily by the severe tapering applied to the specularity gathers.

5. CONCLUSIONS

We applied two formulations of specularity to separate diffractions from reflection data in anisotropic media. The difference between these two formulations, illustrated on a simple isotropic model, suggests that tapering should be adjusted depending on the way one computes the specularity. Both formulations are valid for arbitrarily anisotropic media and can be used to generate images with pure-mode and mode-converted diffractions. High-quality diffraction-based depth images for a VTI ramp model illustrate the potential of presented approach. This methodology performed equally well on the complex VTI Marmousi model where it succeeded in focusing scatterers along the fault planes. A test

for scatterers embedded in a homogeneous VTI medium illustrates the influence of distortions in the velocity field on specularity analysis and imaging of diffractions. However, the stability and accuracy of specularity-based diffraction processing in the presence of errors in the anisotropic velocity model requires further analysis.

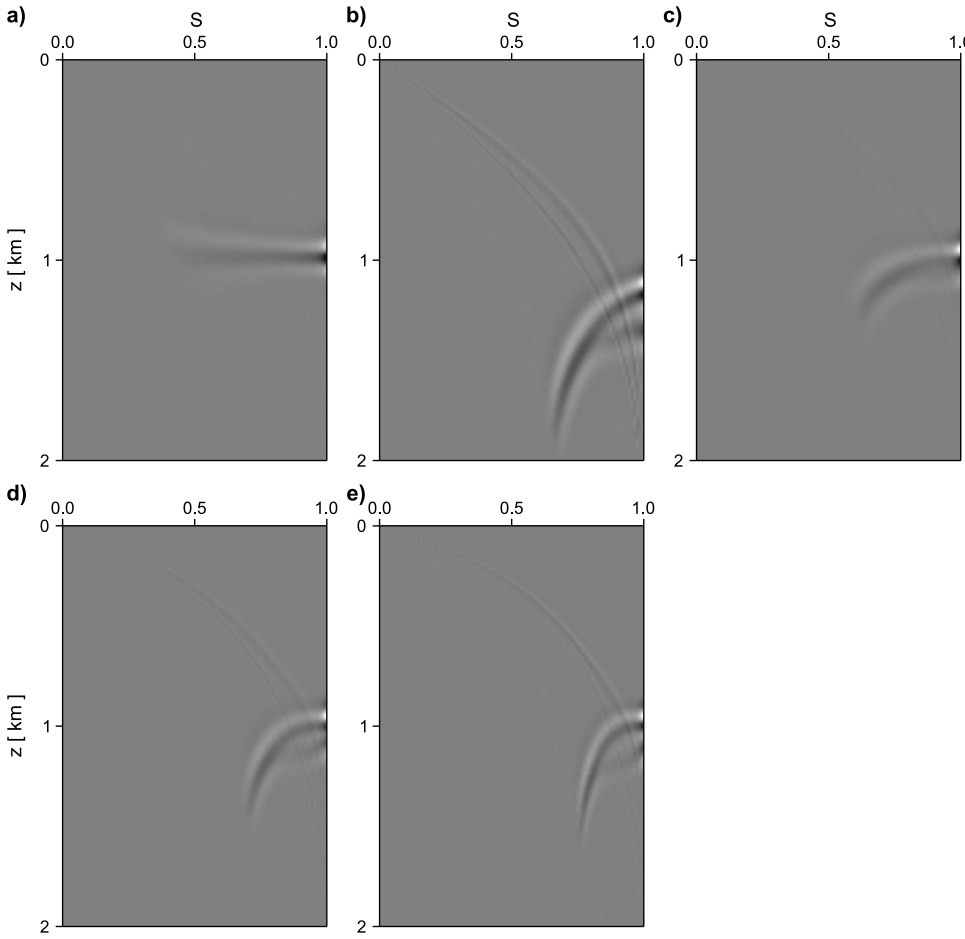

Fig. 10. Specularity (S) gathers for the model in Fig. 8 at location $x = 3.0$ km generated with **a)** the actual velocity field, **b)** the distorted $V_{P0} = 3.5$ km/s, **c)** the distorted $\eta = 0.09$, **d)** the distorted $\eta = 0.16$, **e)** the distorted $\eta = 0.24$.

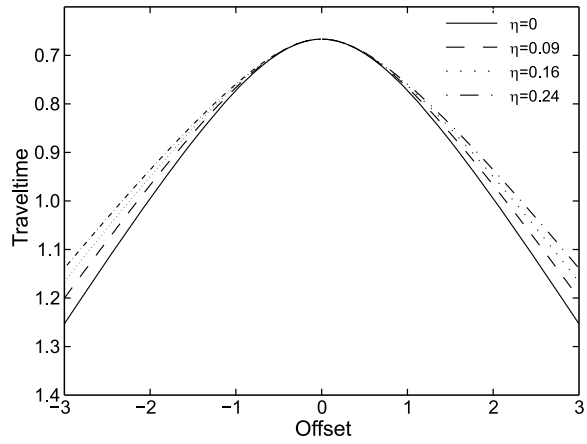

Fig. 11. Diffraction traveltimes for a range of η values computed for the scatterer at location x = 3.0 km and z = 1.0 km (Fig. 8). The shot (x = 3.0 km) and receivers are located at the surface.

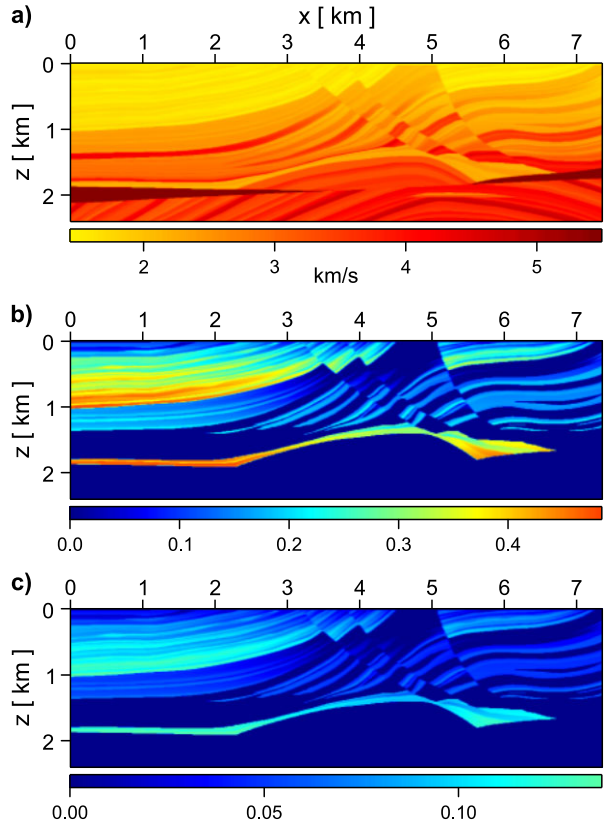

Fig. 12. Parameters for the VTI (transversely isotropic with a vertical symmetry axis) Marmousi model: **a)** V_{P0}, **b)** ε, and **c)** δ.

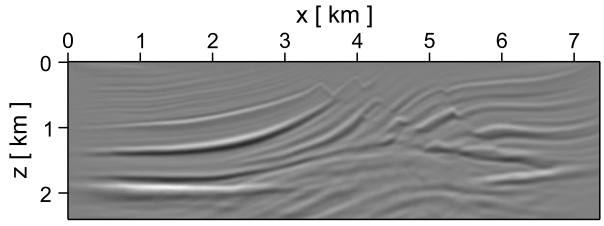

Fig. 13. Depth (z) image of the model from Fig. 12 obtained with the actual velocity field.

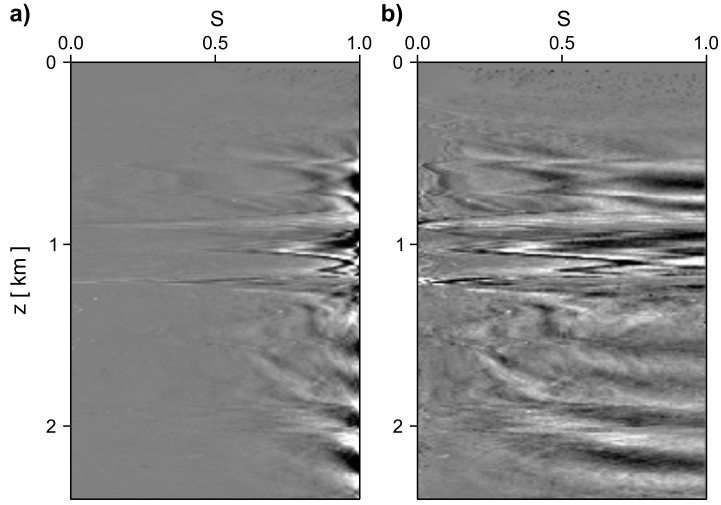

Fig. 14. Specularity (S) gather for the VTI (transversely isotropic with a vertical symmetry axis) Marmousi model at location x = 4.61 km generated with **a)** Eq. (1), and **b)** Eq. (2).

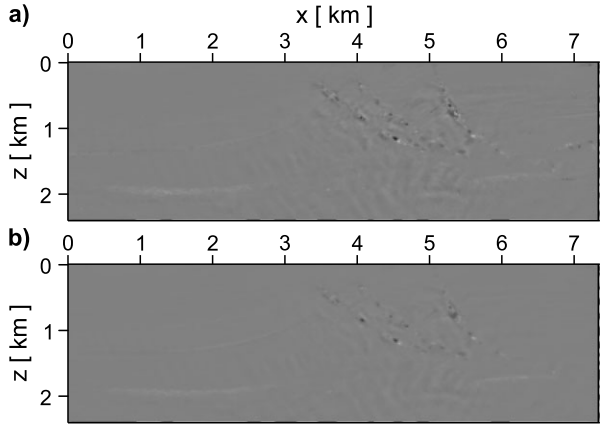

Fig. 15. Depth (z) images from diffractions computed using the specularity defined in **a)** Eq. (1), and **b)** Eq. (2).

Acknowledgments: We are grateful to the members of A(anisotropy)-Team and iTeam at CWP and to Dr. Tijmen Jan Moser of Moser Geophysical Services for useful discussions. The reviews by Tariq Alkhalifah (KAUST) and Evgeny Landa (Tel Aviv University) helped us improve the paper. This work was supported by the Consortium Project on Seismic Inverse Methods for Complex Structures at CWP. The reproducible numeric examples are generated with the Madagascar open-source software package freely available from http://www.ahay.org.

References

Al-Dajani A. and Fomel S., 2010. Fractures detection using multi-azimuth diffractions focusing measure: is it feasible? *SEG Technical Program Expanded Abstracts 2010*, 287–291, DOI: 10.1190/1.3513443.

Alkhalifah T., 1997. *An Anisotropic Marmousi Model*. Stanford Exploration Project SEP-95, 265–282 (http://sepwww.stanford.edu/public/docs/sep95/tariq3/paper_html/).

Berkovitch A., Belfer I., Hassin Y. and Landa E., 2009. Diffraction imaging by multifocusing. *Geophysics*, **74**, WCA75–WCA81.

Chen J., 2004. Specular ray parameter extraction and stationary-phase migration. *Geophysics*, **69**, 249–256.

Fomel S., Landa E. and Taner M., 2007. Poststack velocity analysis by separation and imaging of seismic diffractions. *Geophysics*, **56**, U89–U94.

Khaidukov V., Landa E. and Moser T.J., 2004. Diffraction imaging by focusing-defocusing: An outlook on seismic superresolution. *Geophysics*, **69**, 1478–1490.

Kozlov E., Barasky N., Korolev E., Antonenko A. and Koshchuk E., 2004. Imaging scattering objects masked by specular reflections. *SEG Technical Program Expanded Abstracts 2004*, 1131–1134, DOI: 10.1190/1.1851082.

Landa E., 2010. Diffractions-yesterday, today, and tomorrow. Extended Abstract. 72nd EAGE Conference and Exhibition incorporating SPE EUROPEC 2010. EAGE Publications, EAGE, Houten, The Netherlands, DOI: 10.3997/2214-4609.201400839.

Moser T.J. and Howard C.B., 2008. Diffraction imaging in depth. *Geophys. Prospect.*, **56**, 627–641.

Schneider W.A., 1978. Integral formulation for migration in two and three dimensions. *Geophysics*, **43**, 49–76.

Sturzu I., Popovici A.M., Tanushev N., Musat I., Pelissier M.A. and Moser T.J., 2013. Specularity gathers for diffraction imaging. Extended Abstract. 75th EAGE Conference & Exhibition incorporating SPE EUROPEC 2013. EAGE Publications, EAGE, Houten, The Netherlands, DOI: 10.3997/2214-4609.20130700.

Waheed U.B., Alkhalifah T. and Stovas A., 2013a. Diffraction traveltime approximation for TI media with an inhomogeneous background. *Geophysics*, **78**, WC103–WC111.

Waheed U.B., Stovas A. and Alkhalifah T., 2013b. Anisotropic parameter inversion in VTI media using diffraction data. *SEG Technical Program Expanded Abstracts 2013*, 299–304, DOI: 10.1190/segam2013-0733.1.